Article

Impact of an Uncertain Structural Constraint on Electrical Resistivity Tomography for Water Content Estimation in Landslides

Jasmin Grifka *,†, Maximilian Weigand, Andreas Kemna and Thomas Heinze †

Department of Geophysics, Institute of Geosciences, University of Bonn, 53113 Bonn, Germany;
mweigand@geo.uni-bonn.de (M.W.); kemna@geo.uni-bonn.de (A.K.); thomas.heinze@rub.de (T.H.)
* Correspondence: jasmin.grifka@rub.de
† Current address: Hydrogeochemistry and Hydrogeology Group, Institute of Geology, Mineralogy and Geophysics, Ruhr-University Bochum, 44801 Bochum, Germany.

Abstract: Geoelectrical methods can be part of early warning systems for landslide-prone hillslopes by giving estimates of the water content distribution. Structurally constrained inversions of geoelectrical data can improve the water content estimation by reducing the smoothness constraint along known lithological boundaries, which is especially important for landslides, as often layers with strongly divergent hydrological parameters and varying electrical signatures are present in landslides. However, any a priori information about those boundaries has an intrinsic uncertainty. A detailed synthetic study and a field investigation are combined to study the influence of misplaced structural constraints and the strength of the smoothness reduction via a coupling coefficient on inversion results of electrical resistivity data. While a well-known lithological boundary with a substantial reduction of the smoothness constraint can significantly improve the inversion result, a flawed constraint can cause strong divergences from the synthetic model. The divergence can even grow above the divergence of a fully smoothed inversion result. For correctly placed structural constraints, a coupling coefficient smaller than 10^{-4} uncovers previously unseen dynamics in the resistivity distribution compared to smoothed inversion results. Uncertain layer boundaries can be included in the inversion process with a larger coupling coefficient to avoid flawed results as long as the uncertainty of the layer thickness is below 20%. The application to field data confirms these findings but is less sensitive to a further reduction of the coupling coefficient, probably due to uncertainties in the structural information.

Keywords: electrical resistivity tomography; structural constraint inversion; water content; landslide; monitoring; early warning

1. Introduction

Landslides are a latent danger in many parts of the world. After heavy rainfall events, increasing pore pressure in hillsides is a common source of slope failure (e.g., [1–3]). As more and heavier rainfalls are expected in future years, the number of massive landslides will increase (e.g., [4–7]). There is a growing demand for observation and analysis tools for risk assessment and early warning to protect residents and infrastructure. Factors regarding the moisture content of the soil are considered to have the highest early warning potential [8] and are essential for hazard estimation (e.g., [9,10]). However, even a small divergence in estimated moisture content can have a significant influence on the stability analysis of a landslide-prone hillslope as bonding forces in the soil change suddenly within a range of a few percentages of saturation (e.g., [9,10]).

So far, measurements often focus on slope movement, water content and pore pressure at discrete points (e.g., [11,12]). In recent years, geophysical methods have been used for areal characterization (e.g., [13–18]) and monitoring (e.g., [19–23]) of landslide-prone

hillslopes. Electric resistivity tomography (ERT) has been especially utilized (e.g., [8,24,25]) due to its capability to estimate water content distribution in the subsurface based on the correlation between electrical bulk resistivity and saturation (e.g., [26,27]). However, ERT suffers from resolution limitations, which enhance the non-uniqueness during the inversion of the data. In the traditional inversion of ERT data, a smoothness constraint is included to overcome non-uniqueness (e.g., [28]). Such a smoothness constraint is based on the assumption of gradually varying electrical properties in the ground, which is valid in many cases but may fall short along lithological boundaries. In a smoothed inversion, sharp boundaries are blurred.

Several studies have shown that the hydrogeophysical interpretation of ERT data sets can be significantly improved when structural information is included in the inversion process (e.g., [29–32]). The smoothness constraint can be discarded to enable sharp resistivity contrasts along known layer boundaries. Structural information can be derived from additional sources such as GPR, seismic studies, boreholes, or (hydro-)geological maps. For example, in the study of Doetsch et al. [29], geological layers were identified using ground penetrating radar (GPR) and included in the ERT inversion process to improve the characterization of an aquifer by identifying layers of different hydraulic properties. Al Halgrey [33] emphasizes that constrained inversion is the only option to achieve satisfactory results for monitoring CO_2 mitigation in an underground reservoir using ERT. Since any a priori information for the inversion process has inherent uncertainties dependent on the source, structural constraints should be applied with caution [34]. Although structurally constrained inversions have become more and more common (e.g., [35–38]), in the context of landslides for moisture content estimation [32], there is yet, to our best knowledge, no systematic study on the impact of an uncertain structural constraint [39].

This work studies the effect of a misplaced structural constraint on the water content estimation in a landslide-prone hillslope. A systematic study with a synthetic model based on an actual landslide is conducted concerning the strength of the decoupling via a coupling coefficient and varying accuracy of the assumed boundary. The findings from the synthetic study are applied to measured data from the field site, and the effect of a varying coupling coefficient on the moisture content estimation is evaluated on the basis of field data.

2. Study Area Dollendorfer Hardt

The studied landslide is located on the southern slope of the hill Dollendorfer Hardt in the Siebengebirge, a hill range formed by volcanic intrusions southeast of Bonn, Germany (Figure 1). The geological basement of the area is formed by lower Devonian shales and superposed by Tertiary sediments. At the transition between Oligocene and Miocene, volcanic activity formed the hills of the Siebengebirge with basaltic and latitic intrusions. Volcanic deposits, mainly trachyte tuffs, and Pleistocene sediments overlay and interfinger with the Tertiary sediments on top of the hills (e.g., [40–42]).

The landslide has an affected area of approximately 30,000 m². Its slope inclination is up to 40° and multiple failures occurred in the last 60 years [41]. The first observed failure in the last century happened in 1958 after construction work for a pathway, followed by heavy rainfall over two weeks [41]. A second major failure occurred in 1972, again after heavy rainfall and a rainy season in late summer. The landslide can be separated into a scar zone with four rotational blocks and visible scarp, a narrow transport zone of approximately 15 m width and an accumulation zone with toe failure and several tongues [43]. The landslide events have been classified as rotational slides near the scar zone, turning into mudflows in the transport zone [42,44]. In both cases, the shear plane was located in the clay layer with low hydraulic conductivity [41]. The latest available data suggests creeping slope movement in response to precipitation in the range of a few centimeters per year [43]. The landslide has been extensively studied in the past, and more detailed information concerning its triggering mechanism, geomorphology and geological cross sections can be found elsewhere (e.g., [41–45]).
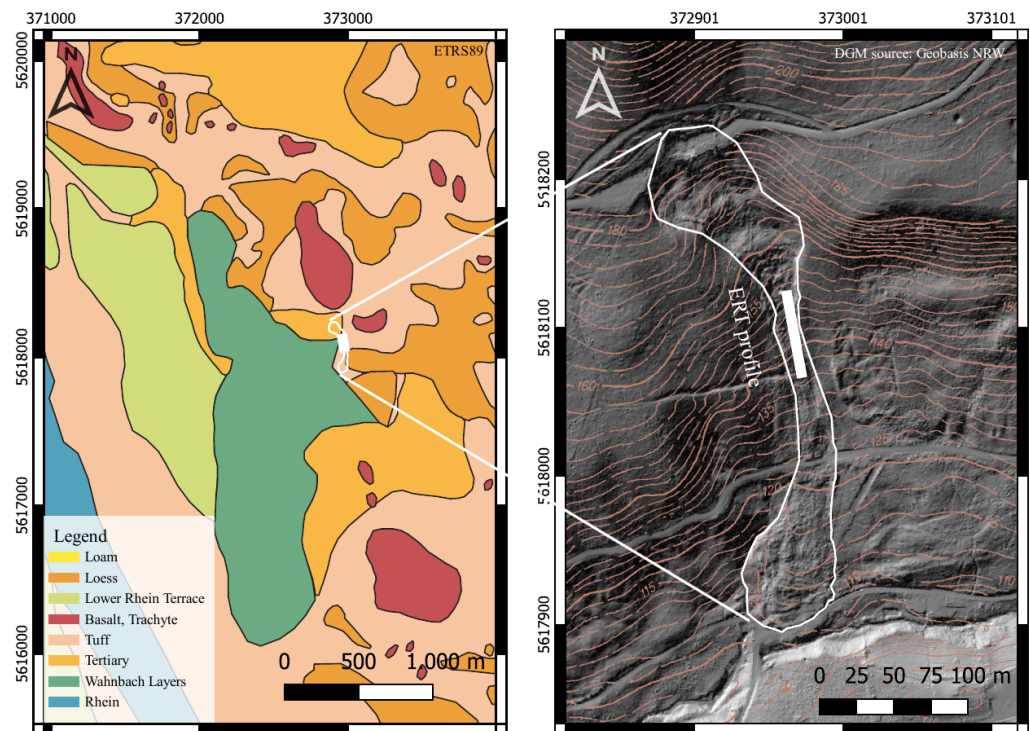
Figure 1. The left map shows a geological map of Dollendorfer Hardt region [46]. The landslide is framed with white on both maps. The right map shows the DEM of the landslide with contour lines for the height above sea level. The ERT profile in the transport zone of the landslide is marked with a white bar.

This study focuses on the transport zone of the previous landslides (Figure 1). Drill logs suggest that the landslide mass lies on top of the Devonian basement at roughly 4 m depth [44]. Original sediments on top of the basement were eroded during the landslide events, and landslide mass was deposited here as the movement stopped. Mineralogical studies of soil probes identified two layers inside the landslide debris [42]. The upper one, down to a depth of 2 m to 3 m, is dominated by trachytic materials, while the lower layer, down to 4 m, shows a high fraction of clay-rich Tertiary sediments [42]. However, the geometry of the landslide is complex, and the landslide material is often mixed and disturbed. A clay content around 65% for the landslide mass and around 30–40% for the Devonian basement has been found [44]. In this part of the slope, a water conductivity of $\sigma_w = 0.1$ S/m was measured in observation wells.

3. Materials and Methods

3.1. Theoretical Background of Constrained Electrical Inversion

Inversions and synthetic modeling in this work are performed with the finite-element-based inversion code CRTomo [47]. During the inversion of ERT data, logarithmic electrical resistivities across the grid cells (model **m**) are iteratively calculated to produce logarithmic resistance values $\mathbf{f(m)}$ comparable to the measured data **d**, assuming uncorrelated and normally distributed errors. In each iteration, the objective function $\psi(\mathbf{m})$, which weights data misfit and model roughness through the regularization parameter λ, is minimized:

$$\psi(\mathbf{m}) = \|\mathbf{W}_d[\mathbf{d} - \mathbf{f(m)}]\|^2 + \lambda \|\mathbf{W}_m \mathbf{m}\|^2, \tag{1}$$

with data weighting matrix $\mathbf{W}_d$ and a matrix $\mathbf{W}_m$ evaluating the first-order roughness of the model vector **m** [47]. The data weighting matrix $\mathbf{W}_d$ is a diagonal matrix with the standard deviation $\epsilon_i = \Delta R_i / R_i$, with resistance error ΔR and resistance R, for the ith of N data points:

$$\mathbf{W}_d = \mathrm{diag}\left\{\frac{1}{\epsilon_1}, ..., \frac{1}{\epsilon_N}\right\}. \tag{2}$$

The maximum value of λ is found through a univariate search at each iteration step, which minimizes the data misfit locally. The iteration stops once the error-weighted data misfit RMS reaches a value close to one:

$$\text{RMS} = \sqrt{\frac{1}{N} \sum_{i=1}^{N} \frac{|d_i - f_i(\mathbf{m})|^2}{|\epsilon_i|^2}}. \tag{3}$$

To avoid overfitting the data, which can cause artifacts in the ERT image, a realistic estimation of the data error ϵ_i is necessary. A resistance error model with parameters a and b for absolute and relative resistance error contributions is used, resulting in a resistance error ΔR for the measured resistance R [48,49]:

$$\Delta R_i = a + bR_i. \tag{4}$$

In a structurally constrained inversion, model roughness between neighboring cells is weighted using a coupling matrix $\mathbf{H}$, which is connected to the model roughness via the Hadamard product. The coupling coefficient η for each element boundary in the matrix $\mathbf{H}$ can vary between fully coupled ($\eta = 1$) and fully decoupled ($\eta = 0$). Along a fully decoupled element boundary, the smoothness constraint is omitted. With the coupling matrix $\mathbf{H}$, the objective function $\psi(\mathbf{m})$ is defined as:

$$\psi(\mathbf{m}) = \|\mathbf{W}_d[\mathbf{d} - \mathbf{f}(\mathbf{m})]\|^2 + \lambda\|\mathbf{H} \odot \mathbf{W}_m \mathbf{m}\|^2. \tag{5}$$

Thus, structural layer boundaries can be considered in the inversion of ERT data through the coupling matrix, assuming that the structural information is relevant for the electrical resistivity distribution in the ground [30]. It has been previously shown that a structural constraint does not introduce an electrical resistivity contrast in the inversion result if not supported by the data [29]. Workflows for the inclusion of external data sources such as ground penetrating radar or refraction seismic are described in detail in Doetsch et al. [29] and Bergmann et al. [30].

3.2. Synthetic Hydraulic and Electrical Modeling

The synthetic model is adapted to the field site and consists of two layers. The upper layer has a thickness of 4 m. Rainwater infiltration was modeled using the 1d—Richard's equation [50] with the Van Genuchten relationship [51]. A 12-hour rain event was simulated at the beginning of a 24-hour period with a spatial discretization of 5 cm and an implicit time stepping of 1 min. Water ponding was avoided by setting the infiltration rate to the maximum value possible by the given hydraulic soil conductivity. For the first layer, the values of the landslide mass were used, and a low hydraulic conductivity of 30 cm/day was assumed. For the Devonian basement layer, a slightly higher hydraulic conductivity of 50 cm/day was used [52]. Further values and parameters were used as listed in Table 1 and were taken from Müller [52].

Table 1. Hydraulic parameters used for the synthetic infiltration modeling.

Symbol	Quantity	Value
$\theta_{sat,1}$	Saturated volumetric water content (layer 1)	0.63
$\theta_{res,1}$	Residual volumetric water content (layer 1)	0.33
α_1	Van Genuchten coefficient (layer 1)	0.027 1/cm
n_1	Van Genuchten exponent (layer 1)	1.21
$K_{sat,1}$	Saturated hydraulic conductivity (layer 1)	30 cm/day
$\theta_{sat,2}$	Saturated volumetric water content (layer 2)	0.45
$\theta_{res,2}$	Residual volumetric water content (layer 2)	0.20
α_2	Van Genuchten coefficient (layer 2)	0.030 1/cm
n_2	Van Genuchten exponent (layer 2)	1.25
$K_{sat,2}$	Saturated hydraulic conductivity (layer 2)	50 cm/day

The calculated saturation S was then used to determine synthetic electrical resistivity values for the two layers assuming a homogeneous infiltration along the electric resistivity profile. The relationship from Waxman and Smits [27] was used to calculate the bulk conductivity σ_b of the soil:

$$\sigma_b = \frac{S^n}{F}\left(\sigma_w + \frac{\sigma_s}{S}\right). \tag{6}$$

All values, including formation factor F and cementation index n for both layers are listed in Table 2. The water conductivity σ_w was taken from field measurements. The surface conductivity σ_s was calculated using the empirical relationship based on clay content cc from Rhoades et al. [53]:

$$\sigma_s = (2.3 \cdot cc - 0.021) \cdot 10^{-3}\,\mathrm{S/m}. \tag{7}$$

This resulted in a resistivity distribution of around $\rho_1 = 20\ \Omega\mathrm{m}$ in the upper, and of $\rho_2 = 100\ \Omega\mathrm{m}$ in the lower layer 24 h after the onset of the synthetic rain infiltration. Apparent electric resistivities (synthetic data) were then calculated for a dipole–dipole configuration with 0, 2, 4 and 6 skipped electrodes in a dipole for a total of 48 electrodes with an electrode spacing of 2.5 m. The finite element grid was set to 134 times 80 rectangular elements covering an area of $167.5 \cdot 20\,\mathrm{m}^2$. The synthetic data were combined with Gaussian noise of 3%. Relative uncertainties for the inversion process were set to 3% accordingly and absolute uncertainties to $10^{-4}\,\Omega$ to account for numerical accuracy.

Table 2. Petro-physical parameters for both layers used for the synthetic study and the field data analysis.

Symbol	Quantity	Value
F_1	Formation factor (layer 1)	4.115
F_2	Formation factor (layer 2)	5.2
n_1	Saturation exponent (layer 1)	1.5
n_2	Saturation exponent (layer 2)	2
σ_w	Pore water conductivity	0.1 S/m
σ_{s1}	Surface conductivity (layer 1)	0.15 S/m
σ_{s2}	Surface conductivity (layer 2)	0.09 S/m

3.3. Data Acquisition and Processing for the Field Case

Electric measurements were taken with a Syscal Pro Switch by IRIS Instruments Inc., Orleans (France), using 48 electrodes with 1 m spacing. A normal and reciprocal dipole–dipole measurement (i.e., exchanging the current and potential dipoles) with 0, 1, 2, 4 and 6 skipped electrodes in a dipole consisting of around 2500 data points each was conducted in April 2017. Due to good quality, no data points were filtered prior to the inversion. The error parameters were set to $a = 10^{-4}\,\Omega$ and $b = 2.5\%$, which is a rather conservative approach for the given data. The inversion was performed using CRTomo [47].

The same profile was analyzed using refraction seismic [45]. The seismic profile was measured with a SUMMIT II Compact by DMT Group, Essen (Germany), using 24 geophones with 2.5 m spacing in December 2016. The seismic profile was significantly longer than the electric profile and was obtained using a roll-along method. Waves were generated by strokes with a 5 kg hammer close to each geophone. For a good signal-to-noise ratio, 10 strokes per geophone were staked. First arrivals were picked, and the wave paths were inverted to gain a tomogram of p-wave velocity V_p using the software ReflexW by J. Sandmeier, Karlsruhe (Germany).

4. Results
4.1. Modeling Results

The effect of a logarithmically varied coupling coefficient η between one and 10^{-6} was investigated using 61 inversions. All other inversion input parameters were similar across

inversions, and all inversions converged to an RMS close to 1. Figure 2 shows the resistivity along a vertical line over 8 m depth in the center of the grid for all conducted inversions. Resistivity contrast between the layers increases with decreasing coupling coefficient. The most visible improvement is for η between 1 and 0.05 when the gradual change in resistivity changes to a sharp contrast. However, $\eta \leq 10^{-4}$ uncovers the heterogeneity in the layers caused by the infiltration process. This is especially visible in the uppermost 2.5 m of the tomogram. Below $\eta = 10^{-4}$, no further change can be observed. The remaining variations between the separate inversions are attributed to fluctuations during the inversion process. For the unconstrained inversion, the relative mean divergence between model and input data is around 30%, while the perfectly matched constrained inversion with $\eta = 10^{-4}$ shows a relative mean divergence of around 5%. The perfectly matched constrained inversion with $\eta = 10^{-3}$ results in a divergence of around 15% since the heterogeneity of the layers is not reproduced.
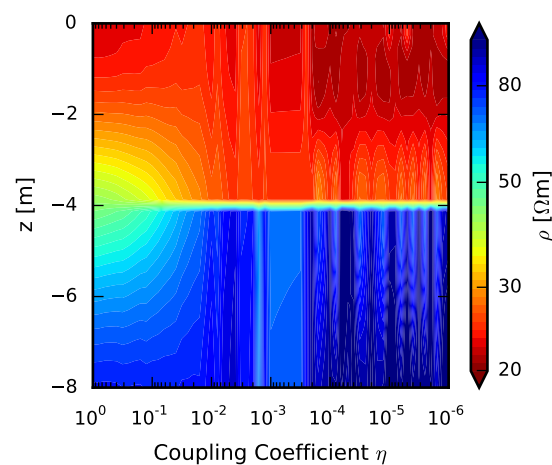

Figure 2. Resistivity profile of 61 inversions with a logarithmic variation of η between one and 10^{-6}.

Structural constraints in the inversion that were shifted relative to the layer boundary in the synthetic model are used to study the influence of a faulty placed constraint. Resistivity along a vertical line over 8 m in the center of the grid for $\eta = 10^{-4}$ is shown in Figure 3a). For comparison, the synthetic model and the smooth inversion result are shown as well. Generally, the discrepancy between the inversion result and the model increases with increasing distance between structural constraint and layer boundary, which is driven by a compensation effect. As the upper layer has a lower resistivity compared to the layer beneath, a structural constraint shifted upwards towards the surface with respect to the layer boundary in the model causes lower resistivities in the inversion result than in the model input in both layers. Vice versa, a downward-shifted constraint causes higher resistivities. This compensation effect becomes vital for growing discrepancies between the constraint and the layer boundary.

Naturally, the region between the structural constraint and the layer boundary has the highest divergence in the resistivities between the inversion result and the model. For the case of a constraint shifted ± 1 m relative to the layer boundary, which corresponds to a quarter of the layer thickness, the maximum local difference in resistivity in comparison to the synthetic model is 120%. Locally, this divergence is much larger than the divergence between an unconstrained inversion and the synthetic model, which shows a maximum deviation of 50%. However, the mean difference between the inversion results with a constraint shifted ± 1 m relative to the layer boundary and the synthetic model along the profile line is below 15%. There are some differences between upward and downward shifted constraints concerning their percent deviation because, in our case, the upper layer has a smaller resistivity so that the percentage difference for upward shifted constrained

inversions is larger than for downward shifted constrained inversions. Considering that, upward and downward shifted constraints have deviations of similar magnitude.
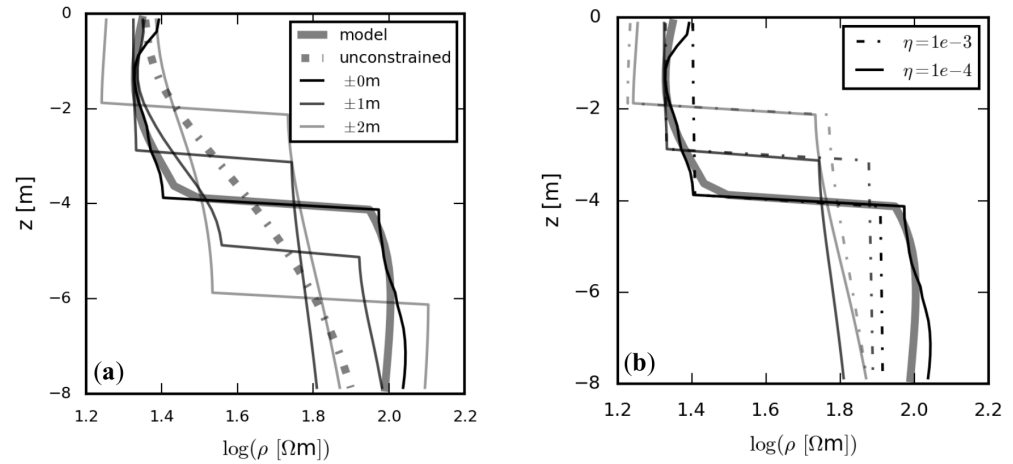
Figure 3. Resistivity along a depth profile in the grid center for misplaced structural constraints using: (**a**) $\eta = 10^{-4}$; and (**b**) varied η.

Besides the absolute difference in resistivities, the degree of resistivity variation within a layer depends on the mismatch between constraint and layer boundary. When the structural constraint is shifted downwards relative to the synthetic model, the resistivity variation in the upper layer is still visible but overestimated. On the other hand, if the structural constraint is shifted upwards, almost no resistivity variation within the layers can be seen. In that case, fewer measurement points for the region above the constraint exist. Therefore, a smaller dynamic range is captured in this region when the constraint is shifted upwards.

The influence of η with respect to misplaced constraints is shown in Figure 3b. If only the deviation in the lower layer is considered for a $+1$ m shifted constraint, the inversion with $\eta = 10^{-3}$ has a maximum divergence of 24% in comparison to 41% for an inversion with $\eta = 10^{-4}$. A further increased coupling coefficient does not result in an even smaller divergence. Therefore, the influence of η seems very limited to compensate for misplaced constraints.
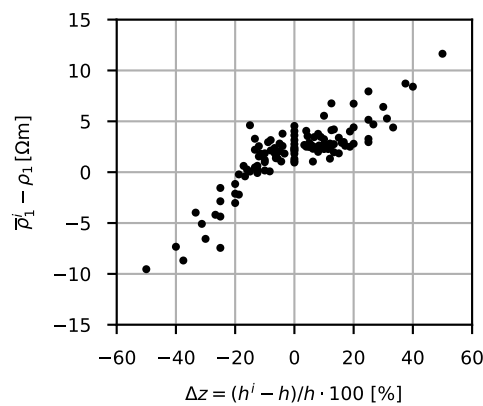

Figure 4. Absolute difference in resistivity between model and inversion result with respect to the difference between layer boundary and structural constraint relative to the thickness of the upper layer.

For generalization, the synthetic model was changed to two homogeneous layers with $\rho_1 = 50$ m and $\rho_2 = 200\ \Omega$m. These values are loosely based on former studies to represent

a typical landslide [15,16,19,54]. The thickness of the upper layer was varied between 2 m and 50 m, and the surrounding grid and measurement layout were adapted accordingly. Input parameters of the inversions were not individually adapted. The coupling coefficient was set to $\eta = 10^{-4}$. The resistivity of the upper layer of the input model ρ_M was compared to the mean value of the upper layer of the inversion result $\bar{\rho}_i$. The grid cells close to the edge and below the structural constraint in the inversion, not the true layer boundary, were excluded from the calculation. The difference between layer depth in the model h and the region above the constraint h' is expressed relative to h. The results, shown in Figure 4, indicate that inversion results tend to overestimate resistivity of the upper layer when its width is overestimated and to underestimate resistivity when its width is underestimated. This agrees with the compensation effect described above but may be different for an inverted resistivity model. However, within a divergence between a true layer boundary and a structural constraint relative to the upper layer thickness of less than 20%, the absolute error is within a narrow margin of 5 Ωm, which is 10% of the layer resistivity in the model. The thicker the upper layer is, the less accurate the structural constraint needs to be placed to achieve a similar agreement with the model. As similar input parameters are used for all inversions, the inversion results overestimate the resistivity even for a perfectly matched constraint. This is within the natural error margin of any inversion using data with noise and could be reduced using adjusted error parameters for each inversion.

4.2. Measurement Results

The seismic data showed three layers, while the fully smoothed ERT inversion resolved only two layers (Figure 5). Due to similar electric conductivities of the materials of the two landslide events, the electric signature of the uppermost layer of trachytic materials is similar to the lower clay-rich materials [42]. However, the elastic properties are diverse enough to be captured with refraction seismic, probably due to compaction during the landslides. The lower layer boundary from the seismic data along a wave velocity isoline of 800 m/s was used as a structural constraint in the ERT inversion.
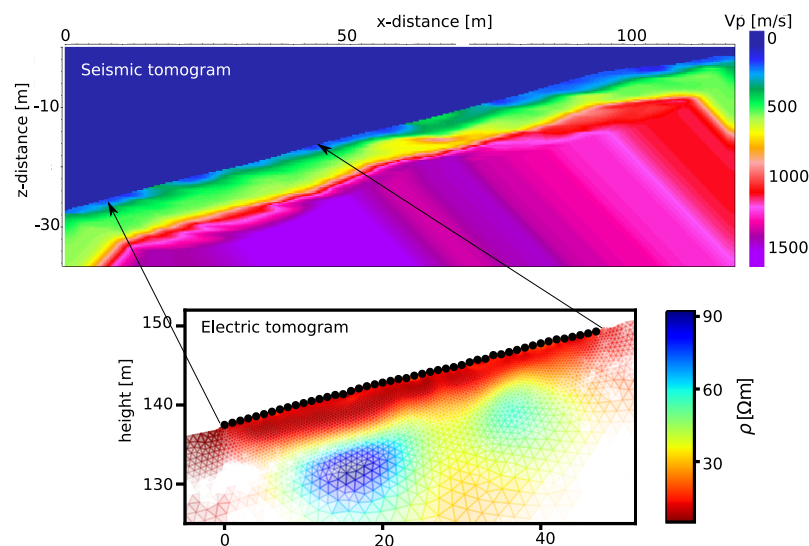
Figure 5. Seismic and unconstrained electric resistivity tomogram.

Constraint inversions of the resistivity data were conducted using varying coupling coefficients. Similar to the results of the synthetic model, an impact of the magnitude of the structural constraint on the resistivity model is visible (Figure 6a–d). The structural constraint uncovers more details of the upper layer (Figure 6c,d) in comparison to the smooth inversion result (Figure 6a). A small resistivity contrast becomes visible within the first layer. Introducing a second structural constraint from the uppermost layer of the seismic tomogram along a wave velocity isoline of 300 m/s in the electric

inversion did not influence the inversion result because the resistivity contrast is too small. Figure 6a–c shows the growing impact of the structural constraint with decreasing coupling coefficient. However, the change from Figure 6c,d is minimal, and no change was observed during further reduction of η. In Figure 6e–g the absolute change in the resistivity compared to the fully smoothed inversion is shown. The emerging heterogeneity in the upper layer with decreasing η is visible. The upper layer separates into two horizontal subregions of higher and lower resistivity. Following the petro-physical relationship (Equation (6)), the volumetric water content is increased in regions of lower electrical resistivity and decreased in regions of higher resistivity (Figure 6). Due to the structural constraint, the corresponding change in volumetric water content is around 4%. Considering the mentioned steep dependence of slope stability on saturation, this could make a significant difference in stability estimations [9,10].
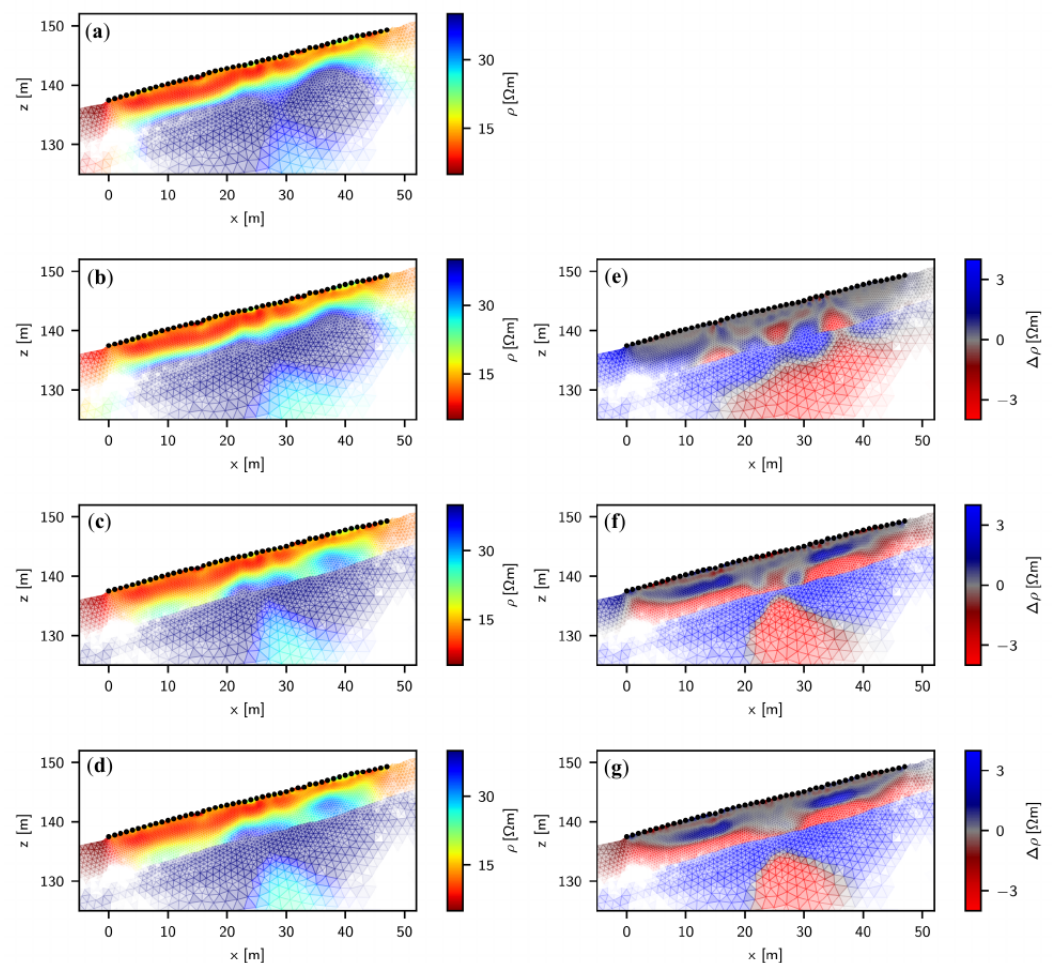
Figure 6. Resistivities (**a–d**) and resistivity differences (**e–g**) compared to the fully smoothed inversion with varying coupling coefficients ($\eta = 1, 0.5, 0.05, 0.005$ from top to bottom row). The colorbar is limited to 40 Ωm to focus on the heterogeneity of the upper layer, but the resistivity in the lower layer reaches up to 100 Ωm.

5. Discussion

The synthetic study shows that the resistivity model and derived moisture contents improve significantly compared to a fully smoothed inversion when the structural constraint in the inversion and the layer boundary match perfectly. The structural constraint matching a sharp resistivity contrast enables the reproduction of this sharp resistivity contrast in the resistivity model in the inversion process more accurately. Without a structural constraint but with the regular smoothness constraint, the range of resistivity values is widened across

a more extensive depth range, thereby falsifying the true resistivity values of this area. Reducing the smoothness constraint at the true location of the sharp resistivity contrast significantly improves the resistivity model and water content estimation.

The magnitude of the smoothness reduction strongly influences the magnitude of the improvement. A reduction of the coupling coefficient from 1 down to 0.05 has the most visible impact on the inversion result due to the change from gradual resistivity distribution to a sharp contrast. This observation from synthetic and field data is in agreement with previous results from Bergmann et al. [30], who find a decoupling of more than 70% necessary to improve time-lapse inversions. In the synthetic model, a further reduction of the smoothness constraint down to $\eta = 10^{-4}$ improves the inversion result concerning the input model by uncovering the heterogeneities within the layers, but only for accurate constraints or slightly thicker top layers. This need for a valid constraint to uncover the full layer heterogeneity might hinder the further improvement of the inversion result for the field data for coupling coefficients below $\eta < 0.005$.

When the structural constraint in the inversion does not represent the layer boundary well, the results can diverge strongly from the synthetic model, even stronger than for a fully smoothed inversion. To compensate for the misplaced boundary, the resistivities of the layers are underestimated for upward shifted boundaries and overestimated for downward shifted boundaries. A spatial accuracy of 25% of the layer position relative to the upper layer thickness is necessary for an error margin below 15% in the resistivity. Heterogeneities within the layers are only reproduced for accurate or slightly downward shifted layer boundaries. Inversions with larger coupling coefficients gain better agreement with the input model for slightly misplaced structural constraints. For large spatial divergence between layer boundary and constraint, this effect vanishes.

As an alternative approach, no structural constraint has to be defined if the ERT data and the geophysical data providing the structural inversion are subjected to a joint inversion (e.g., [55,56]), thus avoiding misplaced constraints while still using all the available information in the most flexible way. However, a constrained inversion has almost no additional computational effort in opposition to a joint inversion. This is especially important when electric resistivity tomography is included as a part of an early warning system for landslides because the processing time is crucial in such a setting. With a usual time window of a few hours between the increase of soil moisture and slope failure, a prolonged processing time for the inversion of geoelectrical data would be a deal breaker. Furthermore, water content dynamics are often monitored using time-lapse measurements, recording multiple measurements within a short time window focusing on dynamic changes in the recorded electrical data (e.g., [57]). For the analysis of time-lapse measurements, it is preferable to have the same a priori information for all inversions because the lithological layer can be considered static while the soil moisture is dynamic. In a joint inversion, the lithological boundary might be shifted each time depending on the sensitivity of the data. Still, a joint inversion might be helpful to initially determine the layer boundary using multiple geophysical methods and then apply the result using a structural constraint for repeated inversions in an early warning system.

6. Conclusions

Quantifying soil moisture content is critical for hazard estimation in pore-pressure-driven slope failure. Electric resistivity methods allow the multi-dimensional spatial acquisition of data points related to soil moisture. However, accurate derivation of moisture content from electrical resistivity requires a priori knowledge about the hydro-geophysical relationship and the extent of the soil layers. Known soil layer boundaries can be included as structural constraints in the electrical inversion by reducing the smoothness constraint along the layer boundary compared to a conventional ERT inversion. This work shows that such a structural constraint can significantly improve moisture content estimations from ERT measurements when the smoothness along the layer boundary is reduced significantly.

As a drawback of the method, any a priori information is affected by uncertainties depending on the data source, and a misplaced structural constraint will negatively influence the inversion process. For strongly misplaced constraints, we find that resulting moisture content estimations can diverge stronger from true values than a fully smoothed inversion. The inversion result can benefit from a higher coupling coefficient in the inversion process to account for uncertainties in the positioning of the structural constraint. In any case, uncertainties in the a priori information must be thoroughly addressed when using a constrained inversion as results can be substantially influenced by flawed constraints. These considerations have to be taken into account when using water content estimations from geoelectrical measurements for landslide early warning systems since small variations in water content can greatly impact stability estimations.

References

1. Lu, N.; Şener Kaya, B.; Wayllace, A.; Godt, J.W. Analysis of rainfall-induced slope instability using a field of local factor of safety. *Water Resour. Res.* **2012**, *48*, W09524. [CrossRef]
2. Gariano, S.L.; Guzzetti, F. Landslides in a changing climate. *Earth-Sci. Rev.* **2016**, *162*, 227–252. [CrossRef]
3. Palmer, J. Creeping earth could hold secret to deadly landslides. *Nature* **2017**, *548*, 384–386. [CrossRef]
4. Highland, L.M.; Bobrowsky, P. *The Landslide Handbook—A Guide to Understanding Landslides*; Technical Report for U.S. Geological Survey: Reston, VA, USA, 2008.
5. Jakob, M.; Lambert, S. Climate change effects on landslides along the southwest coast of British Columbia. *Geomorphology* **2009**, *107*, 275–284. [CrossRef]
6. Petley, D.N. On the impact of climate change and population growth on the occurrence of fatal landslides in South, East and SE Asia. *Q. J. Eng. Geol. Hydrogeol.* **2010**, *43*, 487–496. [CrossRef]
7. Saez, J.L.; Corona, C.; Stoffel, M.; Berger, F. Climate change increases frequency of shallow spring landslides in the French Alps. *Geology* **2013**, *41*, 619–622. [CrossRef]
8. Baron, I.; Supper, R. Application and reliability of techniques for landslide site investigation, monitoring and early warning—Outcomes from a questionnaire study. *Nat. Hazards Earth Syst. Sci.* **2013**, *13*, 3157–3168. [CrossRef]
9. Lu, N.; Likos, W.J. Suction Stress Characteristic Curve for Unsaturated Soil. *J. Geotech. Geoenviron. Eng.* **2006**, *132*, 131–142. [CrossRef]
10. Lu, N.; Godt, J.W.; Wu, D.T. A closed-form equation for effective stress in unsaturated soil. *Water Resour. Res.* **2010**, *46*, 1–14. [CrossRef]
11. Clark, A.; Moore, R.; Palmer, J. Slope monitoring and early warning systems: Application to coastal landslide on the south and east coast of England, UK. In *Landslides*; Senneset, Ed.; Balkema: Rotterdam, The Netherlands, 1996; pp. 1531–1538.
12. Intrieri, E.; Gigli, G.; Mugnai, F.; Fanti, R.; Casagli, N. Design and implementation of a landslide early warning system. *Eng. Geol.* **2012**, *147–148*, 124–136. [CrossRef]
13. Mauritsch, H.J.; Seiberl, W.; Arndt, R.; Römer, A.; Schneiderbauer, K.; Sendlhofer, G.P. Geophysical investigations of large landslides in the Carnic Region of southern Austria. *Eng. Geol.* **2000**, *56*, 373–388. [CrossRef]
14. Lapenna, V.; Lorenzo, P.; Perrone, A.; Piscitelli, S.; Sdao, F.; Rizzo, E. High-resolution geoelectrical tomographies in the study of Giarrossa landslide (southern Italy). *Bull. Eng. Geol. Environ.* **2003**, *62*, 259–268. [CrossRef]

15. Göktürkler, G.; Balkaya, C.; Erhan, Z. Geophysical investigation of a landslide: The Altindag landslide site, Izmir (Western Turkey). *J. Appl. Geophys.* **2008**, *65*, 84–96. [CrossRef]

16. Sass, O.; Bell, R.; Glade, T. Comparison of GPR, 2D-resistivity and traditional techniques for the subsurface exploration of the Öschingen landslide, Swabian Alb (Germany). *Geomorphology* **2008**, *93*, 89–103. [CrossRef]

17. Jongmans, D.; Bièvre, G.; Renalier, F.; Schwartz, S.; Beaurez, N.; Orengo, Y. Geophysical investigation of a large landslide in glaciolacustrine clays in the Trièves area (French Alps). *Eng. Geol.* **2009**, *109*, 45–56. [CrossRef]

18. Chambers, J.; Wilkinson, P.; Kuras, O.; Ford, J.; Gunn, D.; Meldrum, P.; Pennington, C.; Weller, A.; Hobbs, P.; Ogilvy, R. Three-dimensional geophysical anatomy of an active landslide in Lias Group mudrocks, Cleveland Basin, UK. *Geomorphology* **2011**, *125*, 472–484. [CrossRef]

19. Piegari, E.; Cataudella, V.; Di Maio, R.; Milano, L.; Nicodemi, M.; Soldovieri, M. Electrical resistivity tomography and statistical analysis in landslide modelling: A conceptual approach. *J. Appl. Geophys.* **2009**, *68*, 151–158. [CrossRef]

20. Lehmann, P.; Gambazzi, F.; Suski, B.; Baron, L.; Askarinejad, A.; Springman, S.; Holliger, K.; Or, D. Evolution of soil wetting patterns preceding a hydrologically induced landslide inferred from electrical resistivity survey and point measurements of volumetric water content and pore water pressure. *Water Resour. Res.* **2013**, *49*, 7992–8004. [CrossRef]

21. Hübner, R.; Heller, K.; Günther, T.; Kleber, A. Monitoring hillslope moisture dynamics with surface ERT for enhancing spatial significance of hydrometric point measurements. *Hydrol. Earth Syst. Sci.* **2015**, *19*, 225–240. [CrossRef]

22. Gance, J.; Malet, J.P.; Supper, R.; Sailhac, P.; Ottowitz, D.; Jochum, B. Permanent electrical resistivity measurements for monitoring water circulation in clayey landslides. *J. Appl. Geophys.* **2016**, *126*, 98–115. [CrossRef]

23. Uhlemann, S.; Hagedorn, S.; Dashwood, B.; Maurer, H.; Gunn, D.; Dijkstra, T.; Chambers, J. Landslide characterization using P- and S-wave seismic refraction tomography—The importance of elastic moduli. *J. Appl. Geophys.* **2016**, *134*, 64–76. [CrossRef]

24. Ling, C.; Xu, Q.; Zhang, Q.; Ran, J.; Lv, H. Application of electrical resistivity tomography for investigating the internal structure of a translational landslide and characterizing its groundwater circulation (Kualiangzi landslide, Southwest China). *J. Appl. Geophys.* **2016**, *131*, 154–162. [CrossRef]

25. Wicki, A.; Hauck, C. Monitoring critically saturated conditions for shallow landslide occurrence using electrical resistivity tomography. *Vadose Zone J.* **2022**, *21*, e20204. [CrossRef]

26. Archie, G. The Electrical Resistivity Log as an Aid in Determining Some Reservoir Characteristics. *Trans. AIME* **1942**, *146*, 54–62. [CrossRef]

27. Waxman, M.; Smits, L. Electrical Conductivities in Oil-Bearing Shaly Sands. *Soc. Pet. Eng. J.* **1968**, *8*, 107–122. [CrossRef]

28. Constable, S.; Parker, R.; Constable, C. Occam's inversion; a practical algorithm for generating smooth models from electomagnetic sounding data. *Geophysics* **1987**, *52*, 289–300. [CrossRef]

29. Doetsch, J.; Linde, N.; Pessognelli, M.; Green, A.G.; Günther, T. Constraining 3-D electrical resistance tomography with GPR reflection data for improved aquifer characterization. *J. Appl. Geophys.* **2012**, *78*, 68–76. [CrossRef]

30. Bergmann, P.; Ivandic, M.; Norden, B.; Rücker, C.; Kiessling, D.; Lüth, S.; Schmidt-Hattenberger, C.; Juhlin, C. Combination of seismic reflection and constrained resistivity inversion with an application to 4D imaging of the CO_2 storage site, Ketzin, Germany. *Geophysics* **2014**, *79*, B37–B50. [CrossRef]

31. Wagner, F.M.; Bergmann, P.; Rücker, C.; Wiese, B.; Labitzke, T.; Schmidt-Hattenberger, C.; Maurer, H. Impact and mitigation of borehole related effects in permanent crosshole resistivity imaging: An example from the Ketzin CO_2 storage site. *J. Appl. Geophys.* **2015**, *123*, 102–111. [CrossRef]

32. Uhlemann, S.; Chambers, J.; Wilkinson, P.; Maurer, H.; Merritt, A.; Meldrum, P.; Kuras, O.; Gunn, D.; Smith, A.; Dijkstra, T. 4D imaging of moisture dynamics during landslide reactivation. *J. Geophys. Res. Earth Surf.* **2016**, *122*, 398–418. [CrossRef]

33. Al Hagrey, S.A. CO_2 plume modeling in deep saline reservoirs by 2D ERT in boreholes. *Lead Edge* **2011**, *30*, 24–33. [CrossRef]

34. Wagner, F.M.; Uhlemann, S. An overview of multimethod imaging approaches in environmental geophysics. In *Advances in Geophysics*; Schmelzbach, C., Ed.; Elsevier: Amsterdam, The Netherlands, 2021; Volume 62, pp. 1–72. [CrossRef]

35. Ellis, R.G.; Oldenburg, D.W. Applied geophysical inversion. *Geophys. J. Int.* **1994**, *116*, 5–11. [CrossRef]

36. Rizzo, E.; Colella, A.; Lapenna, V.; Piscitelli, S. High-resolution images of the fault-controlled High Agri Valley basin (Southern Italy) with deep and shallow electrical resistivity tomographies. *Phys. Chem. Earth Parts A/B/C* **2004**, *29*, 321–327. [CrossRef]

37. Günther, T.; Rücker, C. A General Approach for Introducing Information into Inversion and Examples from DC Resistivity Inversion. In Proceedings of the Near Surface 2006—12th EAGE European Meeting of Environmental and Engineering Geophysics, Helsinki, Finland, 4–6 September 2006; pp. 1–4. [CrossRef]

38. Merz, K.; Maurer, H.; Rabenstein, L.; Buchli, T.; Springman, S.M.; Zweifel, M. Multidisciplinary geophysical investigations over an alpine rock glacier. *Geophysics* **2016**, *81*, WA147–WA157. [CrossRef]

39. Jiang, C.; Igel, J.; Dlugosch, R.; Müller-Petke, M.; Günther, T.; Helms, J.; Lang, J.; Winsemann, J. Magnetic resonance tomography constrained by ground-penetrating radar for improved hydrogeophysical characterization. *Geophysics* **2020**, *85*, JM13–JM26. [CrossRef]

40. Fuchs, K.; von Gehlen, K.; Mälzer, H.; Murawski, H.; Semmel, A. (Eds.). *Plateau Uplift*; Springer: Berlin/Heidelberg, Germany, 1983. [CrossRef]

41. Hardenbicker, U. *Hangrutschungen im Bonner Raum*; Dümmler: Bonn, Germany, 1996.

42. Schmidt, J.; Dikau, R. Preparatory and triggering factors for slope failure: analyses of two landslides in Bonn, Germany. *Z. Geomorphol.* **2005**, *49*, 121–138.

43. García, A.; Hördt, A.; Fabian, M. Landslide monitoring with high resolution tilt measurements at the Dollendorfer Hardt landslide, Germany. *Geomorphology* **2010**, *120*, 16–25. [CrossRef]

44. Schmidt, J. The role of mass movements for slope evolution—Conceptual approaches and model applications in the Bonn area. Ph.D. Thesis, University of Bonn, Bonn, Germany, 2001.

45. Moradi, S.; Heinze, T.; Budler, J.; Gunatilake, T.; Kemna, A.; Huisman, J.A. Combining Site Characterization, Monitoring and Hydromechanical Modeling for Assessing Slope Stability. *Land* **2021**, *10*, 423. [CrossRef]

46. Nienhaus, U. Geologische und hydrogeologische Verhältnisse im südlichen Siebengebirgsgraben und deren Bedeutung für die Grundwassernutzung und den Grundwasserschutz. Ph.D. Thesis, Technische Hochschule Aachen, Aachen, Germany, 1990.

47. Kemna, A. *Tomographic Inversion of Complex Resistivity: Theory and Application*; Der Andere Verlag: Uelvesbüll, Germany, 2000; p. 169.

48. LaBrecque, D.J.; Miletto, M.; Daily, W.; Ramirez, A.; Owen, E. The effects of noise on Occam's inversion of resistivity tomography data. *Geophysics* **1996**, *61*, 538–548. [CrossRef]

49. Slater, L.; Binley, A.; Daily, W.; Johnson, R. Cross-hole electrical imaging of a controlled saline tracer injection. *J. Appl. Geophys.* **2000**, *44*, 85–102. [CrossRef]

50. Richards, L.A. Capillary Conduction of liquids through porous mediums. *Physics* **1931**, *1*, 318–333. [CrossRef]

51. Van Genuchten, M.T. A Closed-form Equation for Predicting the Hydraulic Conductivity of Unsaturated Soils1. *Soil. Sci. Soc. Am. J.* **1980**, *44*, 892. [CrossRef]

52. Müller, L. *Spezielle Geologische und Geotechnische Untersuchungen bei der Sanierung von Rutschungen im Nördlichen Siebengebirge*; RWTH Aachen: Aachen, Germany, 1987; p. 234.

53. Rhoades, J.D.; Manteghi, N.a.; Shouse, P.J.; Alves, W.J. Soil Electrical Conductivity and Soil Salinity: New Formulations and Calibrations. *Soil Sci. Soc. Am. J.* **1989**, *53*, 433. [CrossRef]

54. Xu, D.; Hu, X.Y.; Shan, C.L.; Li, R.H. Landslide monitoring in southwestern China via time-lapse electrical resistivity tomography. *Appl. Geophys.* **2016**, *13*, 1–12. [CrossRef]

55. Günther, T.; Rücker, C. A New Joint Inversion Approach Applied to the Combined Tomography of DC Resistivity and Seismic Refraction Data. In Proceedings of the 12th EAGE European Meeting of Environmental and Engineering Geophysics (Near Surface 2006), Helsinki, Finland, 4–6 September 2006; p. 039. [CrossRef]

56. Doetsch, J.; Linde, N.; Coscia, I.; Greenhalgh, S.A.; Green, A.G. Zonation for 3D aquifer characterization based on joint inversions of multimethod crosshole geophysical data. *Geophysics* **2010**, *75*, G53–G64. [CrossRef]

57. Haaken, K.; Furman, A.; Weisbrod, N.; Kemna, A. Time-Lapse Electrical Imaging of Water Infiltration in the Context of Soil Aquifer Treatment. *Vadose Zone J.* **2016**, *15*, 1–12. [CrossRef]